

Density Functional Calculations, Electronic Structure, and Optical Properties of Molybdenum Bimetallic Nitrides $\text{Pt}_2\text{Mo}_3\text{N}$ and $\text{Pd}_2\text{Mo}_3\text{N}$

Ali Hussain Reshak,^{*,†,‡} S. Auluck,[§] and I. V. Kityk^{||}

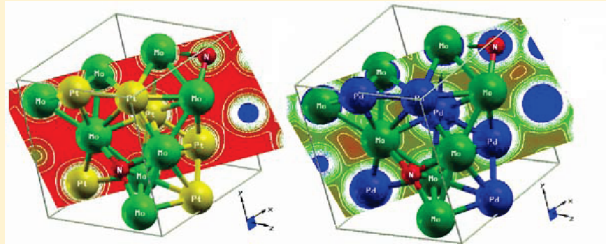
[†]Institute of Physical Biology, South Bohemia University, Nove Hrady 37333, Czech Republic

[‡]School of Microelectronic Engineering, University Malaysia Perlis (UniMAP), Block A, Kompleks Pusat Pengajian, 02600 Arau Jejawi, Perlis, Malaysia

[§]National Physical Laboratory, Dr. K. S. Krishnan Marg, New Delhi 110012, India

^{||}Electrical Engineering Department, Czestochowa University of Technology, Al. Armii Krajowej 17/19, Czestochowa, Poland

ABSTRACT: The electronic band structure, origin of chemical bonds, and dispersion of linear optical susceptibilities for $\text{Pt}_2\text{Mo}_3\text{N}$ and $\text{Pd}_2\text{Mo}_3\text{N}$ have been investigated within the framework of density functional theory (DFT). The atomic positions of $\text{Pt}_2\text{Mo}_3\text{N}$ and $\text{Pd}_2\text{Mo}_3\text{N}$ crystalline compounds taken from the X-ray diffraction data (El-Himri, A.; Marrero-Lopez, D.; Nunez, P. *J. Solid State Chem.* 2004, 177, 3219) were optimized by minimization of the forces acting on the atoms using a full potential linear augmented plane wave (FLAPW) method. We employed the generalized gradient approximation (GGA) of Perdew, Burke, and Ernzerhof (PBE). The DFT calculations show that these compounds have metallic origin with strong orbital hybridization near the Fermi energy level (E_F). The calculated density of states (DOS) at the Fermi energy (E_F) is about 1.83 and 1.02 states/Ry cell, and the bare linear low-temperature electronic specific heat coefficient (γ) is found to be 0.32 and 0.18 mJ/mol·K² for $\text{Pt}_2\text{Mo}_3\text{N}$ and $\text{Pd}_2\text{Mo}_3\text{N}$, respectively. The Fermi surface of $\text{Pt}_2\text{Mo}_3\text{N}$ ($\text{Pd}_2\text{Mo}_3\text{N}$) is composed of three (five) sheets. The bonding features of the compounds are analyzed using the electronic charge density contour in the (110) crystallographic plane. The linear optical properties are calculated with and without the Drude term.



I. INTRODUCTION

The molybdenum bimetallic nitride $\text{Pt}_2\text{Mo}_3\text{N}$ and $\text{Pd}_2\text{Mo}_3\text{N}$ crystalline compounds have been grown by ammonolysis of the stoichiometric amorphous precursor, obtained by freeze drying of aqueous solutions of the appropriate metal salts.¹ The crystals were characterized by elemental analysis, energy-dispersive analysis of X-rays, and X-ray diffraction. The transition metal nitrides, oxynitrides, and carbides have received considerable attention in the field of catalysis owing to the exceptional reactivity shown by some of them² and due to the increasing number of applications of these materials.² Following the mechanical and chemical properties³ and structural versatility of these materials new phases were discovered with novel optical, electrical, magnetic, and chemical properties.^{4–10} Alconchel et al.¹¹ developed a new approach for the synthesis of molybdenum bimetallic nitrides and oxynitrides based on the use of precursors resulting from freeze drying of aqueous solutions of the appropriate common metal salts. Recently, Errandonea et al.¹² studied by means of high-pressure X-ray diffraction the structural stability of $\text{Ni}_2\text{Mo}_3\text{N}$, $\text{Co}_3\text{Mo}_3\text{N}$, and $\text{Fe}_3\text{Mo}_3\text{N}$. They reported ab initio modeling of the high-pressure properties of these compounds and $\text{Pt}_2\text{Mo}_3\text{N}$ and $\text{Pd}_2\text{Mo}_3\text{N}$ using density functional theory (DFT) and density functional perturbation theory (DFPT) with the local density approximation (LDA) for the exchange-correlation energy

implemented in the VASP package. They find that these compounds are good candidates for being incompressible and mechanically stable due to their dense packing and presence of short N–Mo bonds.¹² Also, they found that these compounds have bulk modulus larger than 300 GPa, and their mechanical parameters suggest that they could be suitable for applications as abrasive and cutting tools as well as scratch-resistant coatings.

As there is no experimental and theoretical information about the electronic band structure, total and partial density of states, optical properties, and electron charge densities of these compounds, we thought it worthwhile to take a look at these compounds and perform calculations that will throw light on the electronic band structure, total and partial density of states, optical properties, and electron charge densities. We, therefore, used the XRD data obtained by El-Himri et al.¹ and optimized the structure by minimization of the forces acting on the atoms. Using the technique of relaxed geometry we addressed ourselves for a comprehensive theoretical investigation of the electronic band structure, total and partial densities of states, electron charge densities, and chemical bonds origin using the full

Received: December 7, 2010

Revised: January 25, 2011

Published: March 15, 2011

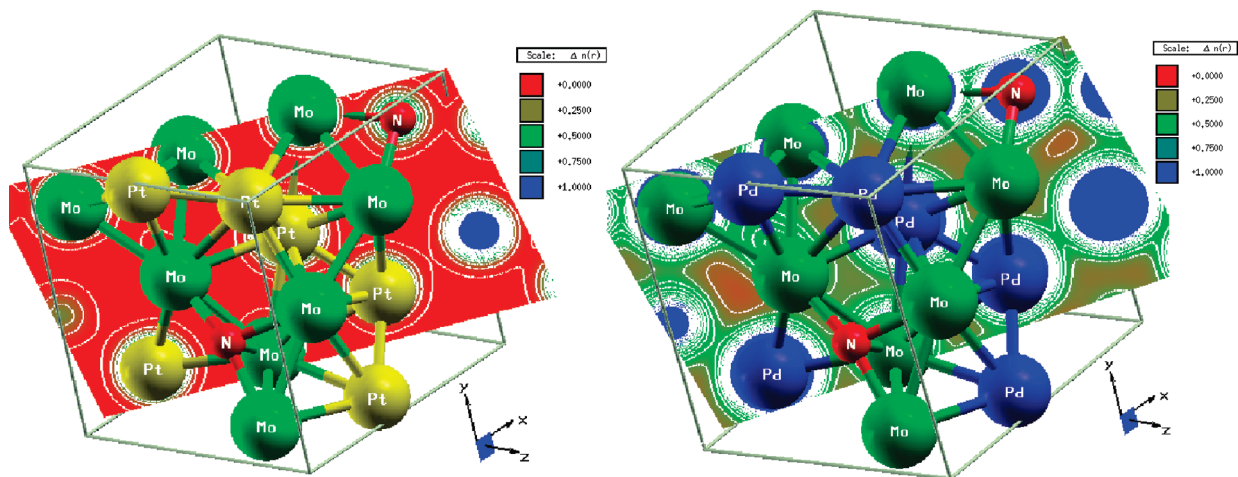


Figure 1. Crystalline structure together with total valence electron charge density distribution along the (110) plane.

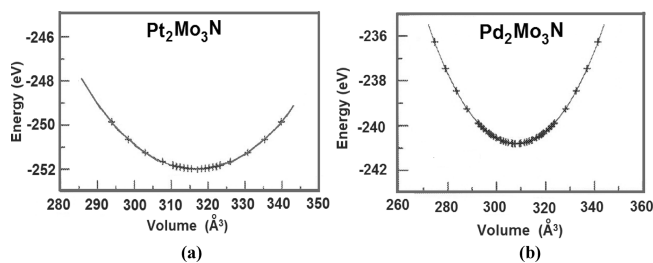


Figure 2. Total energy versus volume.

potential linear augmented plane wave (FP-LAPW) method which has proven to be a reliable method^{13,14} for computation of the electronic structure of solids within a framework of DFT.

In section II we present the basic theoretical aspects of the calculation method. The calculated band structure, density of states, and charge density distributions are given in section 3; section IV is devoted to summarizing our conclusion.

II. THEORETICAL CALCULATION

The X-ray diffraction data and X-ray structural analysis of El-Himri et al.¹ show that the $\text{Pt}_2\text{Mo}_3\text{N}$ and $\text{Pd}_2\text{Mo}_3\text{N}$ single crystals possess the cubic space group $P4132$ (213) with lattice parameters of $a = 6.83586(4)$ and $6.82542(3)$ Å, respectively. The crystals are stable under air up to 580 K, and oxidation is complete at 910 K. The crystalline structures of these compounds are shown in Figure 1.

We performed calculations using the all-electron full potential linearized augmented plane wave (FP-LAPW) method to solve the Kohn–Sham DFT equations within the framework of the WIEN2K code.¹⁵ This is an implementation of the DFT approach¹⁶ with different possible approximations for the exchange correlation (XC) potentials. We employed the generalized gradient approximation (GGA) by Perdew, Burke, and Ernzerhof (PBE),¹⁷ which is based on exchange-correlation energy optimization to calculate the total energy.

We calculated the total energy versus unit cell volume of $\text{Pt}_2\text{Mo}_3\text{N}$ and $\text{Pd}_2\text{Mo}_3\text{N}$ compounds as shown in Figure 2. From the energy volume curves obtained from the full potential calculations the equilibrium volume, bulk modulus, and derivatives of bulk modulus are obtained using a fourth-order

Birch–Murnaghan EOS.¹⁸ These parameters are listed in Table 1, in comparison with the existing experimental data^{19,20} and other theoretical calculations.¹² We should emphasize that these compounds possess high bulk modulus larger than 300 GPa, indicating that they are hard materials in agreement with the experimental data, which indicate that these materials are ultraincompressible.¹² We find that our results show slightly better agreement with the experimental data than the theoretical results of Errandonea et al.¹² We corrected the values of $B_0'' - (\text{GPa})^{-1}$ reported by Errandonea et al.¹² in Table 1. They are -0.0156 ($\text{GPa})^{-1}$ for $\text{Pt}_2\text{Mo}_3\text{N}$ and -0.0183 ($\text{GPa})^{-1}$ for $\text{Pd}_2\text{Mo}_3\text{N}$ from the equation $B_0'' = -[(B_0' - 4)(B_0' - 3) + 35/9]/B_0$, the second pressure derivative of the bulk modulus in a third-order truncation of the Birch–Murnaghan EOS.

We optimized the structure by minimization of the forces (1 mRy/au) acting on the atoms using the theoretical lattice parameter as obtained from the curves. From the relaxed geometry the electronic structure and chemical bonding can be determined and various spectroscopy parameters can be simulated and compared with experimental data. Once the forces are minimized in this construction one can then find the electronic properties by turning off the relaxations and driving the system to achieve self-consistency.

To achieve energy eigenvalues convergence, the wave functions in the interstitial regions were expanded in plane waves with a cutoff $K_{\max} = 9/R_{\text{MT}}$, where R_{MT} denotes the smallest atomic sphere radius and K_{\max} gives the magnitude of the largest K vector in the plane wave expansion. The muffin-tin radii were assumed to be 2.41 atomic units (au) for Pt, 2.13 au for Mo, and 1.89 au for N. The valence wave functions inside the spheres were expanded up to $l_{\max} = 10$, while the charge density was Fourier expanded up to $G_{\max} = 12$ (au)⁻¹. Self-consistency was achieved by use of 1000 k points in the Brillouin zone (BZ). The band structure, densities of states, and optical properties were calculated using 5000 k points of the BZ. The self-consistent calculations were considered to be converged when the total energy of the system is stable within 10^{-5} Ry.

Since the molybdenum bimetallic nitride $\text{Pt}_2\text{Mo}_3\text{N}$ and $\text{Pd}_2\text{Mo}_3\text{N}$ crystallize in the cubic structure, the dielectric tensor has only one principal component. The interband transitions of the dielectric function((ω)) are usually presented as a superposition of direct and indirect transitions. One can neglect the

Table 1. Calculated V_0 (\AA^3), B_0 , B_0' , and B_0'' Using Full Potential Method in Comparison with Experimental Data^{19,20} and Other Theoretical Values¹²

crystal	V_0 (\AA^3)	B_0 (GPa)	B_0'	B_0'' (GPa) ⁻¹
$\text{Pt}_2\text{Mo}_3\text{N}$	319.43 ^a (exp), 314.966 ^b (theory) 317.54 ^d	341.80 ^b (theory) 342.91 ^d	4.81 ^b (theory) 4.90 ^d	-0.020 ^b (theory) -0.016 ^d
$\text{Pd}_2\text{Mo}_3\text{N}$	316.89 ^c (exp), 310.046 ^b (theory) 314.84 ^d	312.11 ^b (theory) 313.16 ^d	4.94 ^b (theory) 4.99 ^d	-0.028 ^b (theory) -0.018 ^d

^a Reference 19. ^b Reference 12. ^c Reference 20. ^d This work. The B_0'' calculated using the formula $B_0'' = -[(B_0' - 4)(B_0' - 3) + 35/9]/B_0$. The values of B_0'' (GPa)⁻¹ obtained by Errandonea et al.¹² are not correct according to the formula $B_0'' = -[(B_0' - 4)(B_0' - 3) + 35/9]/B_0$ and the values of B_0 and B_0' obtained by Errandonea et al.,¹² the correct values should be -0.0156 (GPa)⁻¹ for $\text{Pt}_2\text{Mo}_3\text{N}$ and -0.0183 (GPa)⁻¹ for $\text{Pd}_2\text{Mo}_3\text{N}$.

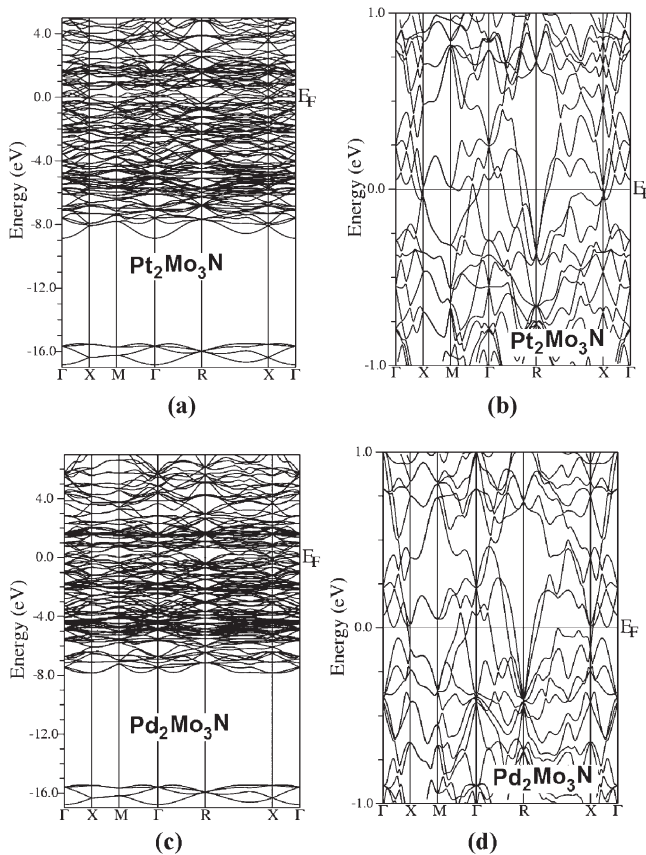


Figure 3. Calculated band structure: (a) full range and (b) enlarged area around the Fermi energy.

indirect interband transitions formed by electron–phonon interactions that are expected to give a small contribution to $\varepsilon(\omega)$.²¹ To calculate the direct interband contributions to the imaginary part of the dielectric function $\varepsilon_2(\omega)$, we carried out summation over all possible transitions from the occupied valence to the unoccupied conduction band states. Taking the appropriate dipole interband transition matrix elements into account, we calculated the dispersion of the imaginary part of the dielectric functions $\varepsilon_2(\omega)$ using the expression²²

$$\varepsilon_2^{ab}(\omega) = \sum_{nm} \int d\vec{k} f_{nm} \frac{\vartheta_{nm}^a(\vec{k}) \vartheta_{mn}^b(\vec{k})}{\omega_{mn}^2} \delta(\omega - \omega_{mn}(\vec{k})) \quad (1)$$

The above expression is written in atomic units with $e^2 = 1/m = 2$ and $\hbar = 1$, where ω is the photon energy and $\omega_{mn}(k)$ is the energy

difference $\omega_{mn}(k) = E_m(k) - E_n(k)$. The integration is performed over the first IBZ. As the investigated compounds are metallic, we included the Drude term (intraband transitions)²³

$$\varepsilon_2(\omega) = \varepsilon_{2\text{inter}}(\omega) + \varepsilon_{2\text{intra}}(\omega) \quad (2)$$

where

$$\varepsilon_{2\text{intra}}(\omega) = \frac{\omega_p \tau}{\omega(1 + \omega^2 \tau^2)} \quad (3)$$

where ω_p is the anisotropic plasma frequency²⁴ and τ is the mean free time between collisions

$$\omega_p^2 = \frac{8\pi}{3} \sum_{kn} \vartheta_{kn}^2 \delta(\varepsilon_{kn}) \quad (4)$$

where ε_{kn} is $E_n(k) - E_F$ and ϑ_{kn}^2 the electron velocity (in the basal plane) squared.

3. RESULTS AND DISCUSSION

3.1. Band Structure, Density of States, Electron Charge Densities, and Fermi Surface. The band structure, total density of states (DOS), along with Pt-s/p/d/f, (Pd-s/p/d), Mo-s/p/d, and N-s/p originated bands are presented in Figures 3 and 4. The DFT calculations show that these compounds have metallic nature with a strong overlap around the Fermi energy (E_F). We find that Pt-s/p/d/f (Pd-s/p/d) states determine the hybridization near E_F with a small admixture of N-p and Mo-s/p/d band states. The DOS at the Fermi energy (E_F) is determined by this overlap (Pt-s/p/d/f, Pd-s/p/d, N-p, and Mo-s/p/d) with a DOS at $E_F - N(E_F) = 1.83$ and 1.02 states/Ry cell for $\text{Pt}_2\text{Mo}_3\text{N}$ and $\text{Pd}_2\text{Mo}_3\text{N}$, respectively. We enlarged the band structure near E_F in order to show the overlapping of the bands around E_F (see Figure 3b and 3d). The electronic specific heat coefficient (γ), which is a function of the density of states, can be calculated using the expression

$$\gamma = \frac{1}{3} \pi^2 N(E_F) k_B^2 \quad (5)$$

where $N(E_F)$ is the DOS at the Fermi energy E_F and k_B is the Boltzmann constant. The calculated density of states at the Fermi energy $N(E_F)$ enables us to calculate the bare electronic specific heat coefficient, which is found to be equal to 0.32 and 0.18 mJ/mol·K² for $\text{Pt}_2\text{Mo}_3\text{N}$ and $\text{Pd}_2\text{Mo}_3\text{N}$, respectively. Following these figures one can see that the band structure and DOS can be divided into two distinct spectral groups/structures. The calculated PDOS (see Figures 3b–i) helps in identification of the angular momentum features of the various structures: (i) in the energy region between -17.0 and -15.0 eV the N-s states show the main contribution with insignificant contribution from

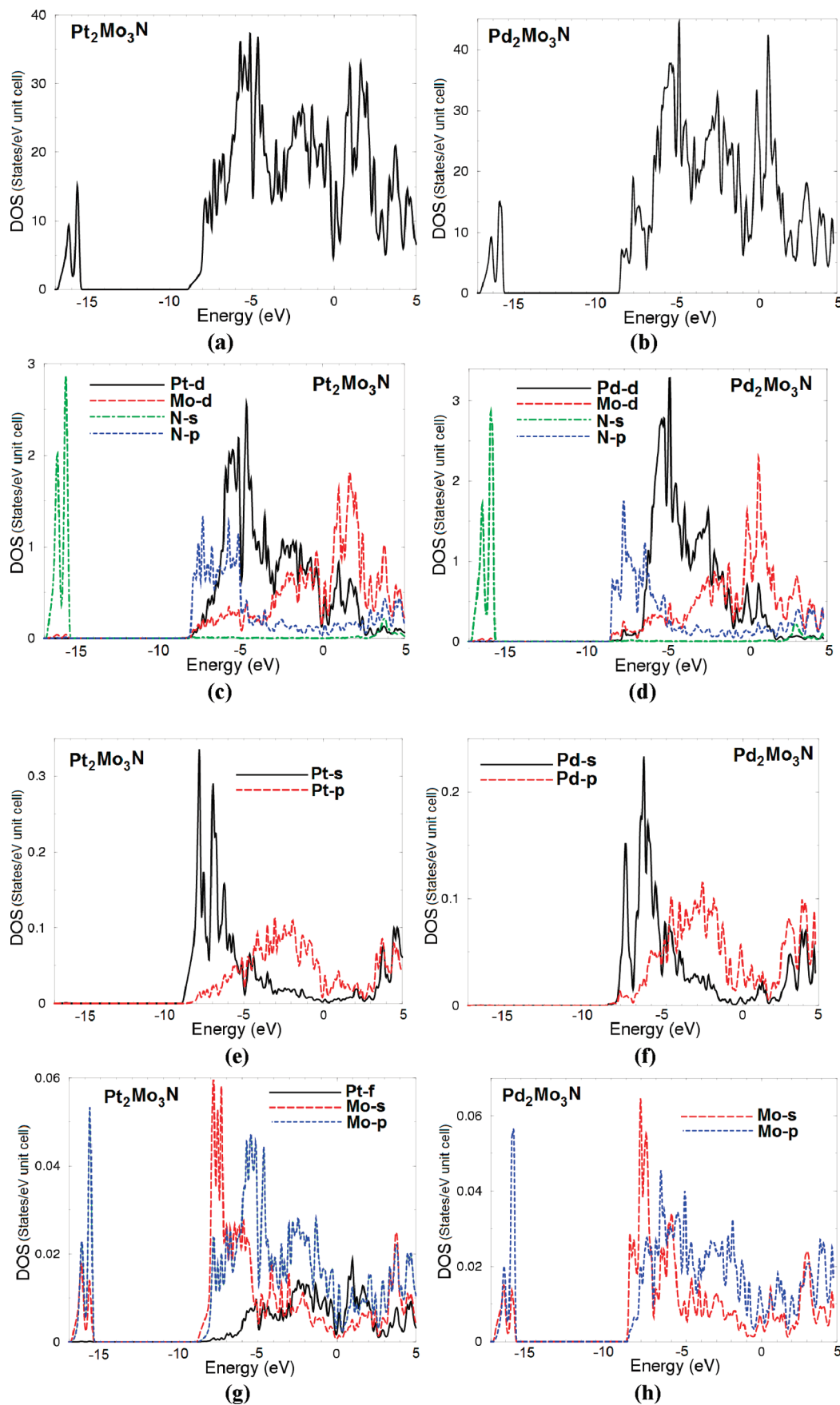


Figure 4. Calculated total and partial densities of states (states/eV unit cell).

Mo-s/p/d states; (ii) in the energy region -8.0 eV and above there is a dominance of Pt-s/p/d/f (Pd-s/p/d), Mo-s/p/d, and N-s/p states. We should emphasize that there is a strong hybridization between the states: (i) at energies between -8.0 and -4.0 eV and 3.0 and 4 eV the Mo-s states strongly hybridized with Mo-p states; (ii) between -5.0 and -4.0 eV N-p states show strong hybridization with Mo-d states; (iii) from -1.0 to 0.5 eV Pt-d (Pd-d) hybridized with Mo-d; (iv) the Pt-f and Mo-p states hybridized strongly in the energy region from E_F to 3.0 eV; (v) at energies between 3.0 and 5.0 eV N-s and Pt-s (Pd-s) hybridized with Pt-d (Pd-d).

The origin of the chemical bonding in $\text{Pt}_2\text{Mo}_3\text{N}$ ($\text{Pd}_2\text{Mo}_3\text{N}$) can be elucidated from the total and partial densities of states. We find that the densities of states, extending from -8.0 eV to the Fermi energy (E_F) are prevailingly originated from Pt-d (Pd-d) states (2.7 electrons/eV) (3.2 electrons/eV), N-p states (1.2 electrons/eV) (1.8 electrons/eV), Mo-d states (1.8 electrons/eV) (2.3 electrons/eV), Pt-s (Pd-s) states (0.31 electrons/eV) (0.23 electrons/eV), Pt-p (Pd-p) states (0.1 electrons/eV) (0.1 electrons/eV), Mo-s states (0.06 electrons/eV) (0.062 electrons/eV), and Mo-p states (0.045 electrons/eV) (0.058 electrons/eV). This is obtained by comparing the total densities of states with the angular momentum projected densities of states of Pt-p/d (Pd-p/d), Mo-s/p/d, and N-p states as shown in Figure 4. These results show that some electrons from Pt-p/d (Pd-p/d), Mo-s/p/d, and N-p states are transferred into valence bands (VBs) and contribute to weak covalence interactions between Pt-Pt (Pd-Pd) and Mo-N atoms.

The bonding properties of the investigated compounds were explained by the investigation of the electronic charge density contours in the (110) plane as shown in Figure 1a and 1b. The contour plots show more ionic and partial covalent bonding between Mo-N which depends on the Pauling electronegativity difference of Mo (1.83) and N (3.0) atoms. As a result, we observe a majority of Mo electronic charge transfer to the N site. This can be seen easily by the color charge density scale where blue (+1.0000) corresponds to the maximum charge accumulation site that is attributed to the fact that Pt has a bigger atomic radius than Pd; hence, the ionization energy and electronegativity of Pd increases. Also, we should emphasize that from the contour plot there is more ionic and partial covalent bonding between Pt-Pt (Pd-Pd) atoms. The charge density along Mo-N and Pt-Pt (Pd-Pd) is pronounced, and this is due to the strong hybridization of covalent Mo-N and Pt-Pt (Pd-Pd) bonds. The interaction between Pt-Mo (Pd-Mo) atoms produces ionic chemical bond and similar for Mo-Mo atoms. We observe that the charge density distribution is essentially spherical around all the atoms. This figure shows clear evidence that the N atom is more electronegative than both Mo and Pt (Pd) atoms, as one can clearly see that the charge accumulates more near N along the Mo-N bond and the charge around N is uniformly distributed.

In condensed matter physics, the Fermi surface determines the low-temperature electronic properties. Hence, it is important to determine the shape of the Fermi surface. The Fermi energy level is determined via the Kohn-Sham eigenvalue of the highest occupied state. Figure 5 shows the Fermi surfaces for the investigated compounds. We should emphasize that there are three bands in $\text{Pt}_2\text{Mo}_3\text{N}$, bands 214 (Figure 5a), 215 (Figure 5b), 216 (Figure 5c), cross the Fermi level, while in $\text{Pd}_2\text{Mo}_3\text{N}$ five bands, bands 164 (Figure 5d), 165 (Figure 5e), band 166 (Figure 5f), band 167 (Figure 5g), and 168 (Figure 5h), cross the Fermi level.

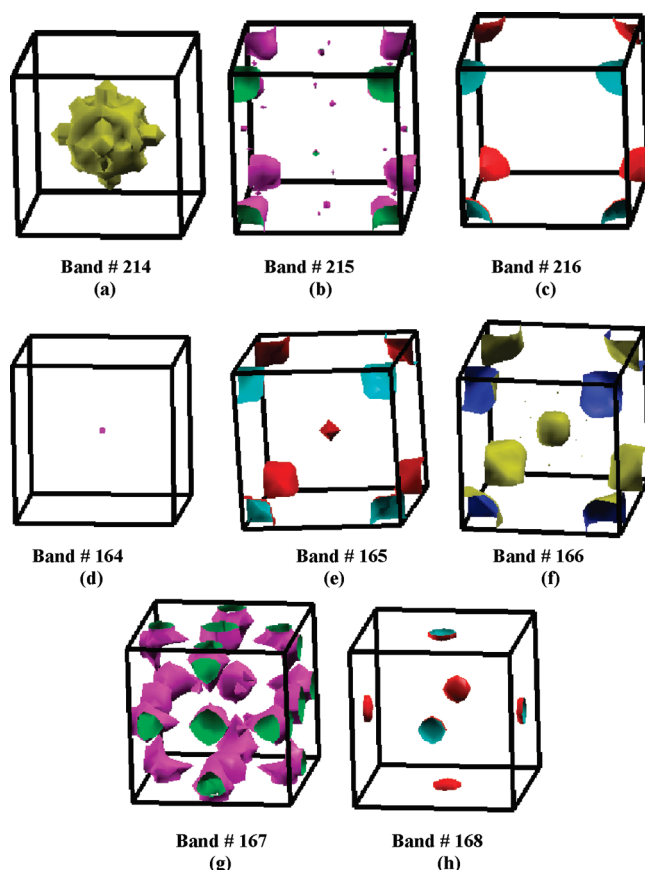


Figure 5. Fermi surfaces for $\text{Pt}_2\text{Mo}_3\text{N}$ at bands 214–216 and $\text{Pd}_2\text{Mo}_3\text{N}$ at bands 164–168.

(Figure 5f), band 167 (Figure 5g), and 168 (Figure 5h), cross the Fermi level.

3.3. First-Order (Linear) Optical Susceptibility Dispersion.

Figure 6a and 6b displays the variation of the imaginary and real parts of the electronic dielectric function $\epsilon(\omega)$. The broadening due to electron-phonon interactions was taken to be equal to about 0.1 eV.²⁵ We performed calculations of $\epsilon(\omega)$ with and without inclusion of the Drude term. The effect of the Drude term is large for energies less than 1 eV. The sharp rise at low energies is caused by the Drude term. The spectral peaks in the optical dispersion are caused by the allowed electric-dipole transitions between the valence and the conduction bands. In order to identify these structures we should consider the values of the optical matrix elements. The observed structures would correspond to those transitions which have large optical matrix dipole transition elements. We noticed that in the imaginary part of the electronic dielectric function of $\text{Pt}_2\text{Mo}_3\text{N}$ there is very strong spectral peak below 2.0 eV; this peak vanishes when we replace Pt by Pd, which is attributed to the fact that Pt has a bigger atomic radius than Pd; hence, the ionization energy and electronegativity of Pd increases. The weakness of the other structures compared to the first peak could be explained by the fact that $\epsilon_2(\omega)$ scales as $1/\omega^2$.

From the imaginary parts of the dielectric function dispersions $\epsilon_2(\omega)$ the real part $\epsilon_1(\omega)$ can be calculated by Kramers-Kronig relations.²⁶ The real part $\epsilon_1(\omega)$ is shown in Figure 6a and 6b. Using the calculated dispersions of the imaginary and real parts of the dielectric function one can evaluate other optical properties

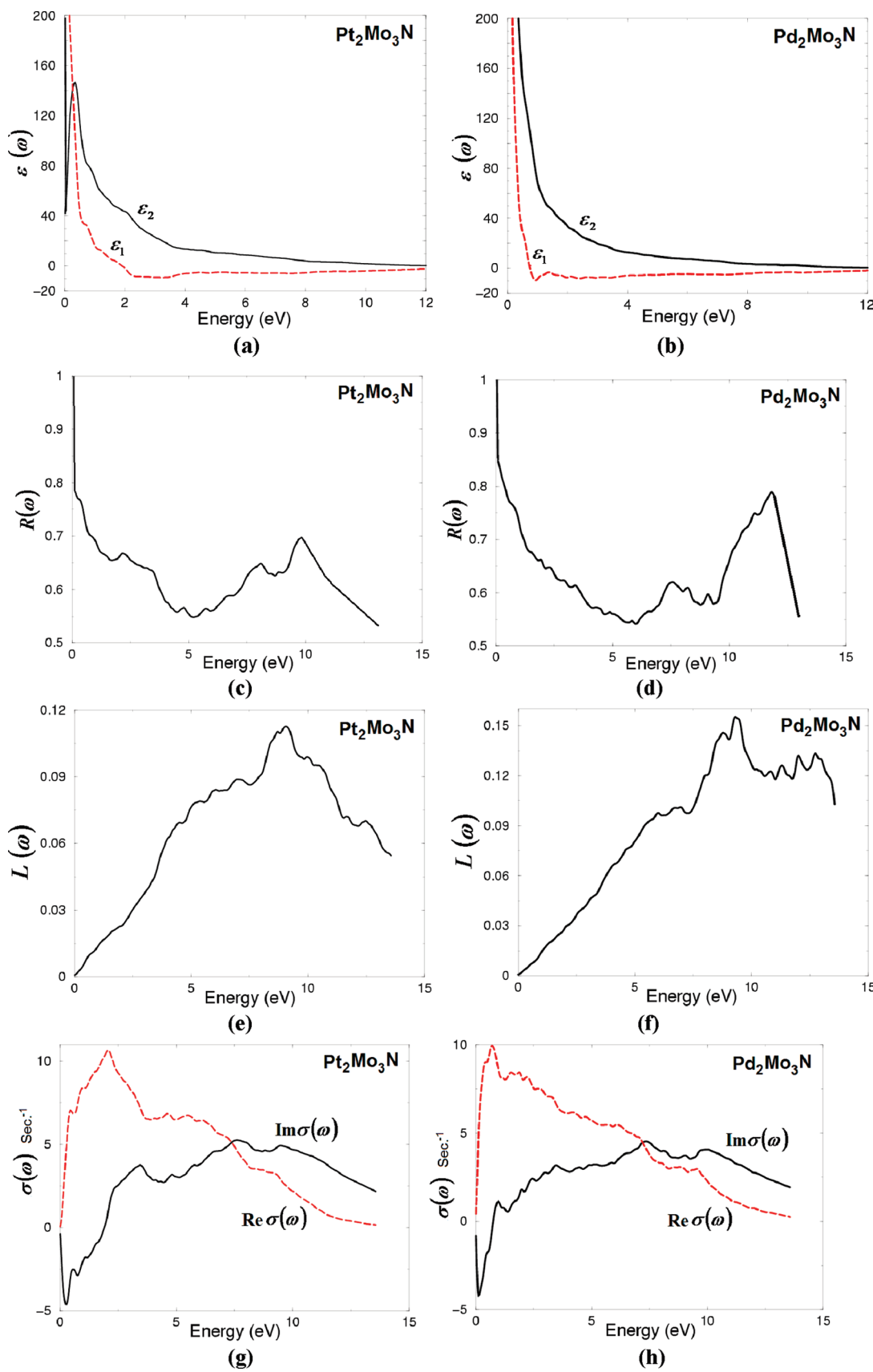


Figure 6. (a and b) Calculated $\varepsilon_2(\omega)$ dispersion (black line) and $\varepsilon_1(\omega)$ (red line). (c and d) Calculated reflectivity spectra $R(\omega)$. (e and f) Calculated loss function $L(\omega)$ spectrum. (g and h) Calculated imaginary part of the conductivity of $\sigma^{xx}(\omega)$ (black line) and real part of the conductivity of $\sigma^{xx}(\omega)$ (red line); the optical conductivity is 10^{15} s^{-1} .

such as reflectivity spectra $R(\omega)$, loss function $L(\omega)$, and conductivity $\sigma(\omega)$.

In Figure 6c and 6d, we present the calculated reflectivity spectra. It is crucial that there is an abrupt reduction in the reflectivity spectrum at 12.5 eV confirming the occurrence of collective plasmon resonance excitations. The depth of the plasmon minimum is determined by the imaginary part of the dielectric function at the plasma resonance and is representative of the degree of overlap between the interband absorption regions. Electron energy loss spectroscopy is a valuable tool to study various aspects of materials.²⁷ The plasmon losses corresponding to a collective oscillation of the valence electrons and their energies are related to the density of valence electrons. In the case of interband transitions, which consist mostly of plasmon excitations, the plasmon excitations give substantial contributions superimposing on the corresponding interband transitions, the scattering probability for volume losses is directly connected to the energy loss function. In Figure 6e and 6f, the energy loss function is plotted in the basal plane and in the direction of the c axis. There are other features in this spectrum, in addition to the plasmon peak, associated with interband transitions. The plasmon peak is usually the most intense feature in the spectrum, and this is at an energy where $\varepsilon_1(\omega)$ goes to zero. The energy of the maximum peak of $(-\varepsilon_1(\omega))^{-1}$ is observed at ~ 9.0 eV for $L(\omega)$, which are assigned to the energy of volume plasmon ω_p . The peak at 9.0 eV is the plasma resonance associated with the collective oscillation of the electrons in the valence band. The other peaks are caused by excitons and other interband transitions. The calculated optical conductivity dispersions $\text{Im } \sigma(\omega)$ and $\text{Re } \sigma(\omega)$ are shown in Figure 6g and 6h. The optical conductivity (OC) is related to the frequency-dependent dielectric function $\varepsilon(\omega)$ as $\varepsilon(\omega) = 1 + (4\pi i \sigma(\omega))/\omega$. The peaks in the optical conductivity spectra are determined by the electric-dipole transitions between the occupied valence band states and the unoccupied conduction states.

IV. CONCLUSIONS

We performed detailed investigations on the electronic band structure, bonding, and dispersion of the linear optical properties of the molybdenum bimetallic nitrides within a framework of DFT based on full potential calculations. The atomic positions of $\text{Pt}_2\text{Mo}_3\text{N}$ and $\text{Pd}_2\text{Mo}_3\text{N}$ are taken from the X-ray diffraction data and optimized by minimization of the forces acting on the atoms using the FP-LAPW method. The investigated compounds possess metallic nature with DOS at a Fermi energy (E_F) equal to about 1.83 and 1.02 states/Ry cell, and the bare electronic specific heat coefficient is found to be 0.32 and 0.18 mJ/mol-K² for $\text{Pt}_2\text{Mo}_3\text{N}$ and $\text{Pd}_2\text{Mo}_3\text{N}$, respectively. We find that three (five) bands determine the shape the Fermi surface of $\text{Pt}_2\text{Mo}_3\text{N}$ ($\text{Pd}_2\text{Mo}_3\text{N}$). The bonding properties were explained by the investigation of the electronic charge density contour in the (110) crystallographic plane. Following the contour plot there is more ionic and partial covalent bonding between Pt–Pt (Pd–Pd) atoms. The charge density along Mo–N and Pt–Pt (Pd–Pd) is pronounced, and this is due to the strong hybridization of covalent Mo–N and Pt–Pt (Pd–Pd) bonds. The interaction between Pt–Mo (Pd–Mo) atoms produces an ionic chemical bond and is similar for Mo–Mo atoms. The linear optical dispersions, namely, the imaginary and real parts of the dielectric function, reflectivity spectra, loss function, and conductivity, were calculated with and without Drude term. We

should emphasize that in the imaginary and real parts of the frequency-dependent dielectric function there is very strong peak below 2.0 eV, and the weakness of the other structures compared to the first peak could be explained by the fact that $\varepsilon_2(\omega)$ scales as $1/\omega^2$.

■ AUTHOR INFORMATION

Corresponding Author

*Phone +420 777729583. Fax. +420-386 361231. E-mail: maalidph@yahoo.co.uk.

■ ACKNOWLEDGMENT

This work was supported by the institutional research concept of the Institute of Physical Biology, UFB (No. MSM6007665808), the program RDI of the Czech Republic, the project CENAKVA (no. CZ.1.05/2.1.00/01.0024), and grant no. 152/2010/Z of the Grant Agency of the University of South Bohemia, The School of Microelectronic Engineering, University Malaysia Perlis (UniMAP), Block A, Kompleks Pusat Pengajian, 02600 Arau Jejawi, Perlis, Malaysia

■ REFERENCES

- (1) El-Himri, A.; Marrero-Lopez, D.; Nunez, P. *J. Solid State Chem.* **2004**, *177*, 3219.
- (2) In *The Chemistry of Transition Metal Carbides and Nitrides*; Oyama, S.T., Ed.; Blackie Academic & Professional, Chapman & Hall: London, 1996. Laurent, Y.; Verdier, P. International Symposium on Nitrides. *J. Eur. Ceram. Soc.* **1997**, *17*, 1773–2037.
- (3) Santhanam, A.T. In *The Chemistry of Transition Metal Carbides and Nitrides*; Oyama, S.T., Ed.; Blackie Academic & Professional, Chapman & Hall: London, 1996; p 28.
- (4) Oyama, T. *S. J. Solid State Chem.* **1992**, *96*, 442.
- (5) Toth, L. E. *Transition Metal Carbides and Nitrides*; Academic Press: New York, 1971.
- (6) Shakelford, J. F. *Introduction to Materials Science for Engineers*; Macmillan: New York, 1988.
- (7) Goldschmidt, H. J. *Interstitial Alloys*; Plenum Press: New York, 1967; pp 214–244.
- (8) Kugler, E.L.; McCandlish, L.E.; Jacobson, A.J.; Chianelli, R.R. U. S. Patent 5138111, 1992.
- (9) Levy, R. B.; Boudart, M. *Science* **1973**, *181*, 547.
- (10) Volpe, L.; Boudart, M. *Catal. Rev. Sci. Eng.* **1985**, *27*, 515.
- (11) Alconchel, S.; Sapina, F.; Beltrain, D.; Beltran, A. *J. Mater. Chem.* **1999**, *9*, 749.
- (12) Errandonea, D.; Ferrer-Roca, Ch.; Martinez-Garcia, D.; Segura, A.; Gomis, O.; Munoz, A.; Rodriguez-Hernandez, P.; Lopez-Solano, J.; Alconchel, S.; Sapina, F. *Phys. Rev. B* **2010**, *82*, 174105.
- (13) Gao, S. *Comput. Phys. Commun.* **2003**, *153*, 190.
- (14) Schwarz, K. *J. Solid State Chem.* **2003**, *176*, 319.
- (15) Blaha, P.; Schwarz, K.; Madsen, G. K. H.; Kvasnicka, D.; Luitz, J. WIEN2K, “an Augmented Plane Wave + Local orbitals program for calculating crystal properties”; Karlheinz Schwarz, Techn. Universitat: Wien, Austria, 2001; ISBN 3-9501031-1-2.
- (16) Hohenberg, P.; Kohn, W. *Phys. Rev. B* **1964**, *136*, 864.
- (17) Perdew, J. P.; Burke, K.; Ernzerhof, M. *Phys. Rev. Lett.* **1996**, *77*, 3865.
- (18) Birch, F. *J. Geophys. Res.* **1978**, *83*, 1257.
- (19) El-Himri, A.; Sapina, F.; Ibanez, R.; Beltran, A. *J. Mater. Chem.* **2001**, *11*, 2311.
- (20) El-Himri, A.; Marrero-Lopez, D.; Nunez, P. *J. Solid State Chem.* **2004**, *177*, 3219.
- (21) Smith, N. V. *Phys. Rev. B* **1862**, *3*, 1971.

- (22) Khan, M. A.; Arti Kashyap, A. K.; Solanki, T.; Nautiyal; Auluck, S. *Phys. Rev. B* **1993**, *23*, 16974.
- (23) Wooten, F., *Optical properties of solids*; Academic Press: New York and London, 1972.
- (24) Kolinko, M. I.; Kityk, I. V.; Krochuk, A. S. *J. Phys. Chem. Solids* **1992**, *53*, 1315–1320.
- (25) Reshak, A. H.; Chen, X.; Auluck, S.; Kityk, I. V. *J. Chem. Phys.* **2008**, *129*, 204111.
- (26) Tributsch, H. *Z. Naturforsch. A* **1977**, *32A*, 972.
- (27) Loughin, S.; French, R. H.; De Noyer, L. K.; Ching, W.-Y.; Xu, Y.-N. *J. Phys. D: Appl. Phys.* **1740**, *29*, 1996.